DOI: 10.1002/ ((please add manuscript number))
Article type: Full Paper

Prussian blue@MoS_2 layer composites as highly efficient cathodes for sodium- and potassium-ion batteries.

Marc Morant-Giner, Roger Sanchis-Gual, Jorge Romero, Antonio Alberola, Leticia García-Cruz, Said Agouram, Marta Galbiati, Natalia M. Padial, João C. Waerenborgh, Carlos Martí-Gastaldo, Sergio Tatay, Alicia Forment-Aliaga and Eugenio Coronado**

M. Morant-Giner, R. Sanchis-Gual, J. Romero, A. Dr. A. Alberola, Dr. L. García-Cruz, Dr. S. Agouram, Dr. M. Galbiati, Dr. N. M. Padial, Dr. J. C. Waerenborgh, Dr. C. Martí-Gastaldo, Dr. S. Tatay, Dr. A. Forment-Aliaga and Prof. E. Coronado
Instituto de Ciencia Molecular, Universitat de València, C/Catedrático José Beltrán 2, Paterna, 46980, Spain
E-mail: alicia.forment@uv.es; eugenio.coronado@uv.es

Dr. J. C. Waerenborgh
Centro de Ciências e Tecnologias Nucleares, Instituto Superior Técnico, Universidade de Lisboa, Bobadela LRS, 2695-066, Portugal

Dr. L. García-Cruz Institute of Electrochemistry, Universidad de Alicante, 03080 Alicante, Spain
Dr. S. Agouram
Department of Applied Physics and Electromagnetism, Universitat de València, Dr. Moliner 50, Burjassot 46100, Spain

Keywords: Prussian blue, MoS_2 layers, sodium-ion batteries, potassium-ion batteries, 2D composites

Prussian blue (PB) represents a simple, economical and eco-friendly system as cathode material for sodium-ion batteries (SIBs). However, structural problems usually worsen its experimental performance thus motivating the search for alternative synthetic strategies and the formation of composites that compensate these deficiencies. Herein, a straightforward approach for the preparation of PB/MoS_2-based nanocomposites is presented. MoS_2 provides a 2D active support for the homogeneous nucleation of porous PB nanocrystals, which feature superior surface areas than those obtained by other methodologies, giving rise to a compact PB shell covering the full flake. The nanocomposite exhibits an excellent performance as cathode for SIBs with discharge capacity values up to 177 $mA \cdot h \cdot g^{-1}$ and a specific

capacitance of 354 $F \cdot g^{-1}$. These values are even larger for the intercalation of K^+ ions (215 $mA \cdot h \cdot g^{-1}$, reaching a specific capacitance of 489 $F \cdot g^{-1}$). Compared to similar composites, superior performance can be ascribed to a synergistic effect of the coordination compound with the 2D material.

1. Introduction

In the highly competitive field of energy storage systems, lithium ion batteries (LIBs) have played a determinant role during last years. [1,2] However, motivated by the limited availability of Li in Earth, batteries based on other more abundant alkaline metals like sodium or potassium have raised enormous interest.[3,4] The quest for alternative systems that can rival with LIBs performance has motivated the study and development of different materials and composites. [5]

PB is a cyanide bridged coordination compound of general formula $A_xFe^{III}[Fe^{II}(CN)_6]_y \cdot \square_{1-y} \cdot nH_2O$ where A is an alkaline metal ion (K^+ or Na^+) and $\square$ represents $[Fe(CN)_6]^{4-}$ vacancies occupied by coordinating water ($0 < x < 1$; $0.75 < y < 1$).[6] PB and its extensive family of analogues (PBAs) form a numerous family of materials that can be easily synthetized in large scale and with cheap and environment-friendly approximations.[7] The interstitial voids present in these coordination polymers permit the accommodation and release of the alkaline cations with a maximum diameter of 3.6 and 4.6 Å, upon reduction and oxidation processes without drastic structural modifications. For instance PB, with a calculated specific capacity close to 170 $mA \cdot h \cdot g^{-1}$,[8,9] has become a popular target material in the preparation of aqueous rechargeable batteries for applications in energy-storage systems.[4,10-12] However, the reported specific capacities until now have usually remained well below this theoretical value. This can be explained due to the existence of structural defects as $[Fe(CN)_6]^{n-}$ vacancies and the inclusion of water molecules as coordinating ligands and/or within interstitial voids, that

complicates alkaline cations diffusion, giving rise to low electronic conductivity, inferior rate capability and poor cycling stability. These features have led to the preparation of PB by means of a countless number of synthetic strategies that sought highly crystalline-defect free coordination compounds.[9] On the other hand, PB has also been integrated into different types of composites with the aim of improving other aspects like stability, homogeneous structuration at the nanoscale, ease of assembly, or enhanced conductivity of the material. [13,14] For example, previous results demonstrate that the formation of small particle size PB crystals uniformly distributed on a conducting carbon matrix can be very beneficial for the electrochemical performance of the system.[14] Small crystals provide shorter diffusion lengths and thus, alkali ions diffusion rates are improved. Moreover, the strain produced by volume changes during ion charge and discharge processes is minimized, which in turn improves rate capability and stability. Besides, as the surface area increases, the contact between the PB and the matrix becomes more efficient, improving electron transport and structural resilience.[14]. In the same direction, materials with high surface-to-mass ratio like graphene and graphene oxide have been used in the design of 2D composites where the 2D material is decorated with PB nanoparticles by reaction with iron precursors in solution, most often assisted by means of the action of a reducing agent.[15,16] In this way, composite sodium ion batteries (SIBs) electrodes, with higher reversible capacities and better cyclability compared to the analogous bare PBs,[13] [17,18] have been prepared with discharge–charge capacity values reaching 160 $mA \cdot h \cdot g^{-1}$ and with a capacity retention at 0.5 C up to 92.2%.[19] However, the use of PB and PBAs composites based on 2D materials different from graphene or its oxide has remained almost unexplored.

MoS_2 is the most studied member of the inorganic laminar transition metal dichalcogenide (TMDC) family.[20] Its electronic properties have motivated the implementation of MoS_2 layers in numerous and different kinds of electronic devices.[21] Additionally, MoS_2 is able to intercalate different metal ions in between its layers and has been extensively used for

electrochemically energy storage devices (LIBs, SIBs and supercapacitors) with outstanding performance, either as bulk material or in the form of chemically exfoliated nanosheets.[22] Moreover, the negative charge in MoS_2^{n-} ($rMoS_2$), resulting from the exfoliation in water of n-butyllithium (*n*-BuLi) reduced MoS_2 (Li_xMoS_2),[23] can be used to promote the functionalization of the 2D material with electrophiles[24,25] and metallic or PB nanoparticles.[26,27] Notwithstanding, the potential synergistic combination of two high performance energy storage materials like PB and exfoliated MoS_2 into a new 2D composite is still a nascent field of research.[27] [28]

Herein, we present a strategy in which chemically exfoliated $rMoS_2$ is used as reducing agent and as platform for the ultrafast crystallization of continuous PB shells (sample **1**). Moreover, we use mechanically exfoliated MoS_2 subjected (sample **2**) or not (sample **3**) to a reducing agent before its functionalization with PB, to highlight that the accumulation of negative charge is essential for the successful growth of the composite. Furthermore, we expose deposited chemically exfoliated $rMoS_2$ networks on silicon substrates to evaluate the charge transfer degree between the components yielding the new hybrid composite (samples **4** and **5**) or to study the transport properties of the new material (sample **6**).

Looking forward the functionality of composite **1** as cathode for K^+ and Na^+ ions batteries, a detailed electrochemical study is presented. Using Na^+ as electrolyte, this new material displays unprecedented discharge capacity values up to 177 $mA \cdot h \cdot g^{-1}$ at current density of 1 $A \cdot g^{-1}$ and specific capacitance of 354 $F \cdot g^{-1}$. These values are even better with K^+ electrolyte, reaching 215 $mA \cdot h \cdot g^{-1}$ with specific capacitance up to 489 $F \cdot g^{-1}$. These numbers exceed theoretical predictions for bare PB, which points out an active role of the 2D precursor. ~~Additionally, we give chemical insight on the composition of the electroactive material and on the selective growth of PB on the $rMoS_2$.~~

2. Results and Discussion

2.1 Composite preparation & Chemical characterization

Suspended thin $rMoS_2$ flakes 1-5 nm thick and 0.2-1.2 μm wide were prepared by the well-known method of *n*-BuLi intercalation,[23] followed by dispersion in water under mild sonication conditions. The quality of the exfoliated material was evaluated by powder X-Ray diffraction (PXRD), UV/Vis, Raman spectroscopy, transmission electron microscopy (TEM) and atomic force microscopy (AFM) (**Figure S1–S3, S5, S6 and S8, S9; Table S1**). As expected, and confirmed by zeta potential[24], *n*-BuLi exfoliated MoS_2 flakes are partially reduced (zeta potentials around -45 mV) and form stable dispersions due to interparticle electrostatic repulsions.[29]

In order to synthesize PB/MoS_2-based composite (**1**), a fresh $rMoS_2$ water dispersion was mixed with a 1:1 50 mM $K_3Fe(CN)_6$: $FeCl_3$ aqueous solution. The mixture was allowed to react for 15 minutes under magnetic stirring, after this time it was filtered and the resulting solid was copiously washed with water in order to remove excess of unreacted iron salts. The PXRD pattern of the isolated dark blue powder collected at room temperature displays characteristic PB peaks (**Figure 1a**).[30,31] Structure and phase purity of PB in **1** was confirmed with a Pawley refinement of the PXRD data by using the standard pattern for tetrairon(III) tris(hexacyanoferrate(II)) tetradecahydrate available from ICSD 1277. Full-profile fit yields acceptable cell parameters, agreement factors and profile differences (a = 10.298 Å, R_p = 1.12, R_{wp} = 1.48%, **Table S2**). Noticeably, no MoS_2 peaks were observed,[27] probably because the functionalization with PB prevents the re-stacking of the layered structure of MoS_2. An average particle size of 11.1 nm was determined from peak (200) FWHM (0.60) using Scherrer analysis. The porous nature of **1** was confirmed by N_2 adsorption-desorption measurements at 77 K (**Figure 1e**). As expected for PB particles, **1** displayed type-IV reversible N_2 uptake with no hysteresis. The calculated values for multi-point Brunauer-

Emmett-Teller (BET), 354 $m^2 \cdot g^{-1}$ and the total pore volume, 0.26 $cm^3 \cdot g^{-1}$ are remarkable. If compared to the use of other 2D templates like reduced graphene oxide,[19] nucleation onto MoS_2 yields PB particles with close to 3 times higher specific surface areas that might translate in superior electrochemical performance due to more favorable ion diffusion. Analysis of the pore size distribution (PSD) by using non-linear solid density functional theory (NLDFT) indicates that porosity is dominated by micropores in accordance with the expected PB mean pore diameter of 5.7 Å at P/P_0 = 0.0-0.3 and intergrain mesoporosity between 0.3 and 0.9 (**Figure 1f**).

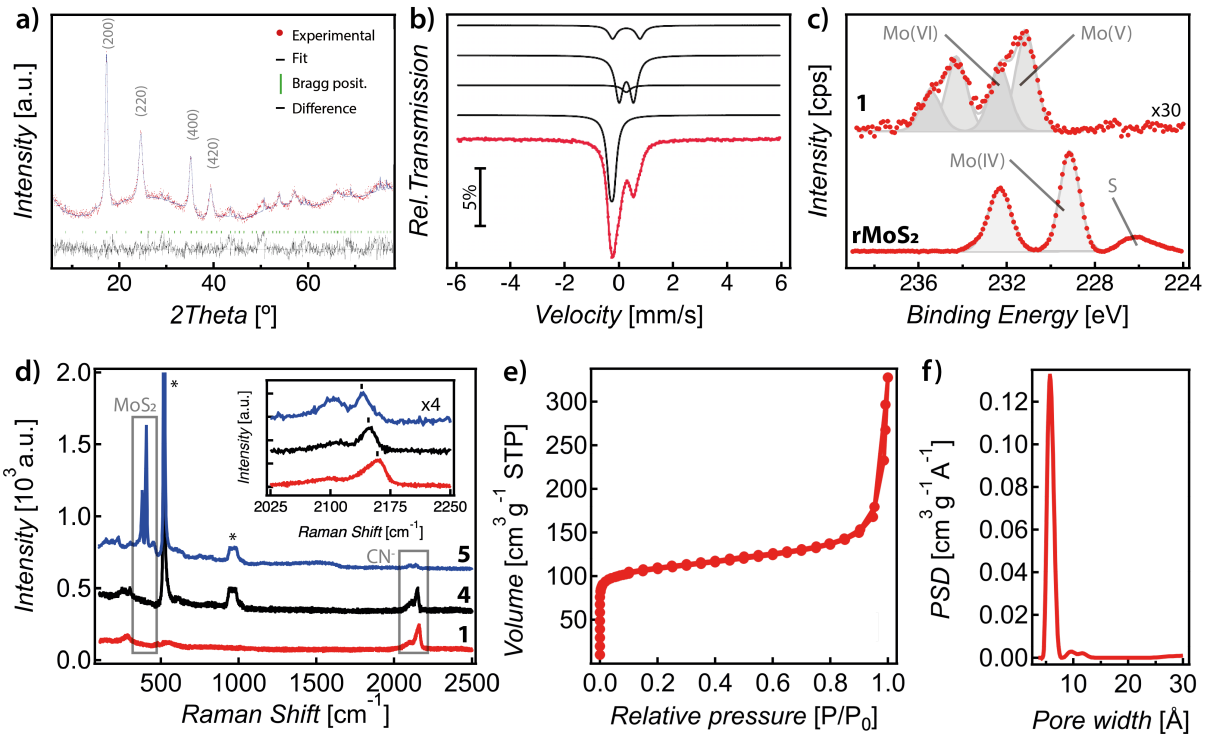

Figure 1. a) Refined powder X-ray diffraction pattern of **1.** Experimental (red dots), calculated (blue line), difference plot [(I_{obs}–I_{calc})] (black line, bottom panel) and Bragg positions (green ticks) for the Pawley refinement; b) Mössbauer spectrum of **1** taken at 295 K. The lines over the experimental points are the sum of 4 doublets (see supporting information) and have been slightly shifted for clarity; c) Mo3d XPS high resolution spectra of **1** (top) and $rMoS_2$; d) Raman spectra of composite **1**(red), and surface samples **4** (black) and **5** (blue), SiO_2 Raman peaks are marked with *; e) N_2 adsorption-desorption isotherm of **1**; f) Pore size distribution of **1**.

As can be seen in Figures 1a (red line) and **S4**, the Raman spectrum of **1** is dominated by PB peaks: a peak at *ca.* 2154 cm^{-1} corresponding to the A_{1g} C≡N stretching vibrational band, a weak peak around 2097 cm^{-1} corresponding to the E_g C≡N stretching vibrational mode and two smaller peaks at 540 and 281 cm^{-1} related to Fe–C stretching modes (**Table S3**).[32-34] No additional peaks related to MoS_2 or MoO_3 can be distinguished. The presence of Fe-coordinated C≡N groups was further confirmed by IR spectroscopy (**Figure S12**), which shows a vibrational band at 2079 cm^{-1} ascribed to the Fe^{II}-C≡N stretching mode, and the bands near 600 and 500 cm^{-1} referred to the Fe^{II}-C≡N-Fe^{III} bending modes. The presence of interstitial water molecules in composite **1** leads to the appearance of two additional bands near 3420 and 1616 cm^{-1}, which are attributed to the O-H stretching and H-O-H bending modes, respectively. [35,36] Based on the redox process used for the growth of PB particles on $rMoS_2$ layers, and due to the fact that the C≡N stretching vibrational bands at the Raman spectra of compound **1** do not show any significant shift respect to the Raman spectrum of bulk PB, and that there are not additional peaks that could be assigned to the formation of new covalent bonds (i.e. ν(S-CN)), we propose non-covalent electrostatic interactions as the most plausible forces between the 2D material and the coordination compound.

The mixed valence nature of the PB in **1** was confirmed by means of Mössbauer spectroscopy (**Figure 1b** and **table S4**). The spectra of **1** are similar to those reported for PB compounds containing both low-spin Fe^{II}, S=0, and high-spin Fe^{III}, S=5/2. [34,37] Using a similar analysis to that reported by Grandjean et al.[34] (see supporting information) a Fe(II)/Fe(III) ratio of ~0.75 was calculated. The K:Fe and Fe:Mo ratios (~0.07 and ~16, repsectively) were determined using inductively-coupled plasma optical emission spectrometry (ICP-OES). X-ray photoelectron spectroscopy (XPS) analysis of the sample (**Figure S15**) shows the presence of all expected peaks, except for that of sulfur (see later). Compared to $rMoS_2$, **(Figure S13**) **1** displays one order of magnitude less intense Mo 3d signal. Moreover, the high-resolution Mo

3d XPS spectrum is dominated by a pair of doublets at 235.5/232.3eV and 234.3/231.1 eV that contribute 40% and 60% to the overall Mo signal, respectively (**Figure S16**). According to the literature, we identify them as coming from Mo(V) and Mo(VI) states (**Figure S14**). [38-40] Noticeably, no appreciable trace of $Mo^{IV}S_2$ states peaking at 229.2 eV and 232.3 eV are visible. Therefore, it would seem that during the reaction $K_3Fe(CN)_6$ overoxidizes $rMoS_2$, presumably to laminar H_xMoO_3[41,42] and/or MoS_yO_x species.[43] This conclusion is further supported by elemental analysis (C17.8%, N19.0%, S1.1%), where only half of the expected sulfur is detected. Finally, thermogravimetric analysis (**Figure S17**) was used to best estimate the water content from the first mass loss (~25%) in the TGA curves (second mass drop above 250ºC is due to PB cyanide loss). Taking into account all this information the composition of **1** can be approximated to $(K_{0.47}Fe_4^{III}[Fe^{II}(CN)_6]_{3.14})@(MoSO_{1.7})_{0.44}\cdot 18H_2O$.

Additionally, magnetic properties of the composite were studied using a SQUID magnetometer (**Figure S18-S20**), confirming that PB displays the characteristic soft magnet behavior, with a long range ferromagnetic order at $T_c \sim 3.5$ K, in good agreement with those expected for the small particle size (*ca.* 11 nm) observed in composite **1**.[44]

Scanning electron (SEM) and transmission electron microscopies (TEM) were performed in order to evaluate the morphology of **1**. As can be seen in **Figures 2**, **S21** and **S22** the composite keeps a lamellar structure with flakes completely covered by a continuous layer of PB nanocrystals. This is in contrast with other PB/2D composites reported in literature that show the presence of isolated cubic PB crystals more or less sparse over the MoS_2 surface. [15,27] Such difference arises from the double role played by $rMoS_2$, both as reducing agent and nucleation platform in the absence of any other surfactant or stabilizing surface agent. This gives rise to a quick nucleation and growth of PB small crystals all over the $rMoS_2$ surface. Fast Fourier transform (FFT) analysis of high-resolution TEM images of the PB NPs revealed a face-centered cubic (fcc) pattern with a = 10.11 Å, in close agreement with PXRD data (Figure 2c). The homogeneous distribution of the cyanoferrometalate network on the flakes is

further confirmed using EDS mapping, where Mo signal is perfectly correlated with Fe, C and N signals (Figure 2d-h, **S7**).

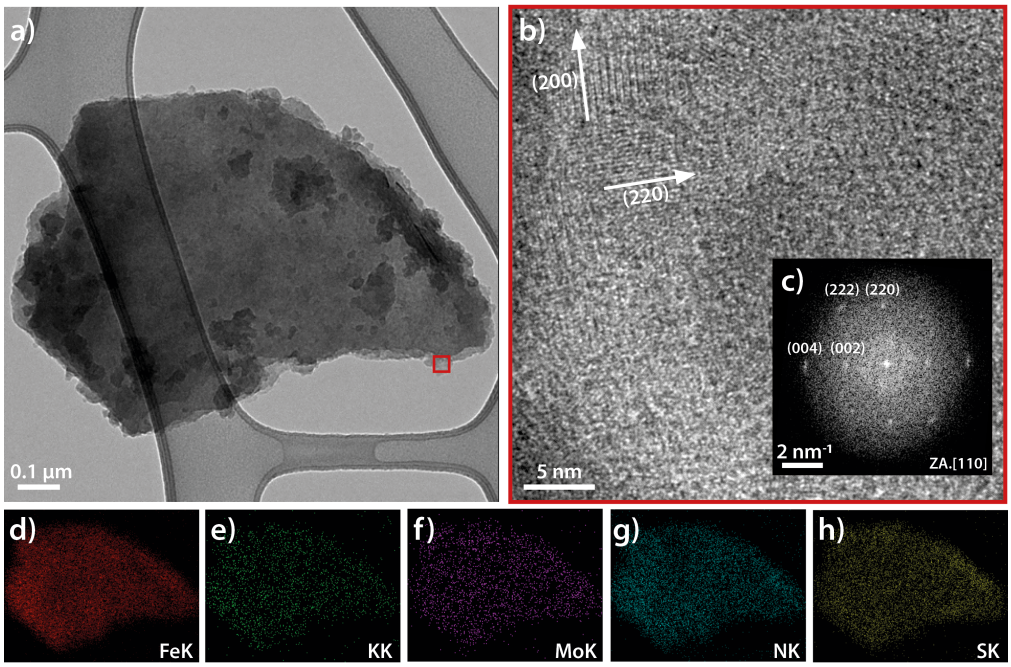

Figure 2. a) TEM image showing a layer uniformly decorated by PB nanoparticles; b) High resolution TEM image of the red squared area in (a); c) Corresponding FFT from (b); (d)-(h) EDS mapping of different elements present in a flake of **1**.

In order to gain a better understanding about the process involved in the composite formation, and to highlight the crucial role played by the negative charges accumulated over the rMoS_2 surface during the PB growth, surface experiments were carried out. First, two mechanically exfoliated MoS_2 thin layers (samples **2** and **3**) were deposited on SiO_2 (285nm)/Si substrates from bulk MoS_2 crystals using mechanical exfoliation[45] and characterized by optical microscopy and AFM. Next, **2** was immersed in *n*-BuLi 1.6 M in hexane for 24 h under inert atmosphere and then copiously rinsed with solvent.[25] Finally, a 1:1 50 mM $K_3Fe(CN)_6$: $FeCl_3$ solution (the same mixture used for the preparation of bulk 2D composite **1**) was spincoated over both samples and microscopy measurements were performed again. As can be seen in **Figure 3** the reduced sample (**2)** developed a very compact PB film of ~40 nm thick, contrary to what is observed on sample **3** which was not reduced with *n*-BuLi (**Figure**

S10). Moreover, this experiment shows that the selective functionalization of MoS_2 layers can be downscaled to the single layer limit.

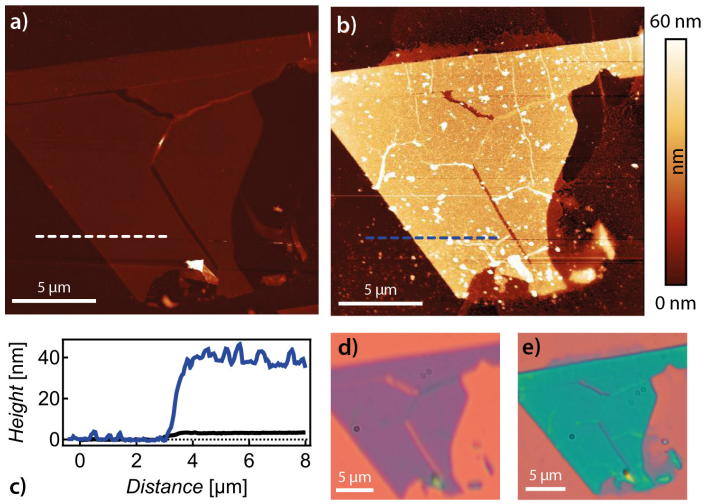

Figure 3. AFM topographic images of a BuLi-treated mechanically exfoliated MoS_2 flake (sample **2**) (a) before and (b) after treatment with a $K_3Fe(CN)_6$: $FeCl_3$ aqueous solution; their height profiles are presented in (c); d) and e) show optical images of the same sample before and after PB functionalization, respectively.

In a next step, to further extend the control over the active deposition area, we tested if PB could be nucleated on $rMoS_2$ layers coating large areas of the surface. Two $rMoS_2$ flake networks (samples **4** and **5**) were first deposited by spin coating freshly dispersed material on SiO_2 (285nm)/Si substrates; in a next step a $K_3Fe(CN)_6$: $FeCl_3$ aqueous solution was spin coated to the surface bound networks. Two Fe concentrations were used during these experiments: a 1:1 50 mM $K_3Fe(CN)_6$: $FeCl_3$ solution for **4** and another one 2.5 times more diluted for sample **5**. In both cases, a continuous thin film of material preferentially grows on top of the flakes after few seconds of reaction with the iron solution, as can be observed by AFM microscopy (**Figure S11**). A clear difference between samples **4** and **5** was observed by confocal Raman spectroscopy (Figure 1a black and blue lines, respectively). Thus, the spectrum recorded for **4** resembles the one of powder sample **1** and displays only PB peaks with no signals related to MoS_2 or its oxide. On the contrary, sample **5** shows the characteristic in-plane E^1_{2g} (*ca.* 382 cm^{-1}) and out-of-plane A^1_g (*ca.* 406 cm^{-1}) MoS_2 signals,

matching the frequency difference expected for thin MoS_2 flakes, 3-4 layers thick.[46] Moreover, in **5** the A^1_g C≡N vibration is less intense and is shifted to lower energies (*ca.* 2040 cm^{-1}). This shift is correlated to a decrease in the average valence state of Fe.[47-49]

The above results seem to confirm our hypothesis that $rMoS_2$ acts as a reducing agent and as a consequence its selective functionalization with cyanoferrometalates only takes a few seconds. When low concentration Fe(III) solutions are used, the amount of deposited material is lower (weak ^1A_g C≡N Raman signals), MoS_2 peaks can be detected and the deposited material is mostly reduced to Fe(II). However, for higher Fe(III) concentrations, thicker shells are formed and the ratio Fe(II)/Fe(III) decreases. At the same time, $rMoS_2$ is oxidized to less crystalline species with higher oxidation states, its characteristic Raman signals are broadened and/or masked by the PB film and eventually lost. The obtained nanocomposite directly nucleated over the surface, opens the door to the fabrication of structured 3D electrodes.[50]

It is also important for the potential applicability of the new hybrid composite to have some knowledge about the pathways that dominate the electronic transport through it. The transport properties of the composite were studied on freshly chemically exfoliated $rMoS_2$ flakes deposited by spin coating over commercial interdigitated pre-patterned Au electrodes (sample **6**) and I-V curves were recorded at room temperature (**Figure S23**, red line). An almost linear response was observed, as expected for $rMoS_2$.[51] [24] Right after this first measurement, a 50 mM $K_3Fe(CN)_6$: $FeCl_3$ solution was spincoated over the samples and transport measurements were performed again. After functionalization, resistance was clearly increased and a semiconductor behavior was observed (black line). Interestingly, the sample showed a completely insulating behavior when it was measured under vacuum (Figure S23, gray line). The same semiconducting/insulating behavior under vacuum is confirmed when 2D composite **1** was dispersed by drop casting over the pre-patterned electrodes. These findings are in concordance with previous reports on solid-state PB electrical properties, where PB is

described as a semiconductor when absorbed moisture is present,[52,53] while it becomes an insulator when it is vacuum dried.[54] Moreover, this measurement points out that, after functionalization, a continuous PB shell covers the flakes and dominates the electrical transport in the solid state.

2.3 2D composite 1 as high-quality Sodium/Potassium-ion battery cathode

In the last part of this paper we will test the performance of composite **1** as potential cathode material for sodium or potassium ion batteries (SIBs and KIBs respectively). The electrochemical performance of the material was evaluated in a typical three-electrode cell by cyclic voltammetry (CV) and galvanostatic charge-discharge cycles at different current densities in three different aqueous solutions of Na_2SO_4 (1 M and 0.5 M) and K_2SO_4 (0.5 M) as electrolytes. In order to reach higher conductivity within the composite in the working electrode, **1** was deposited on a carbon felt previously calcinated at 1000ºC.

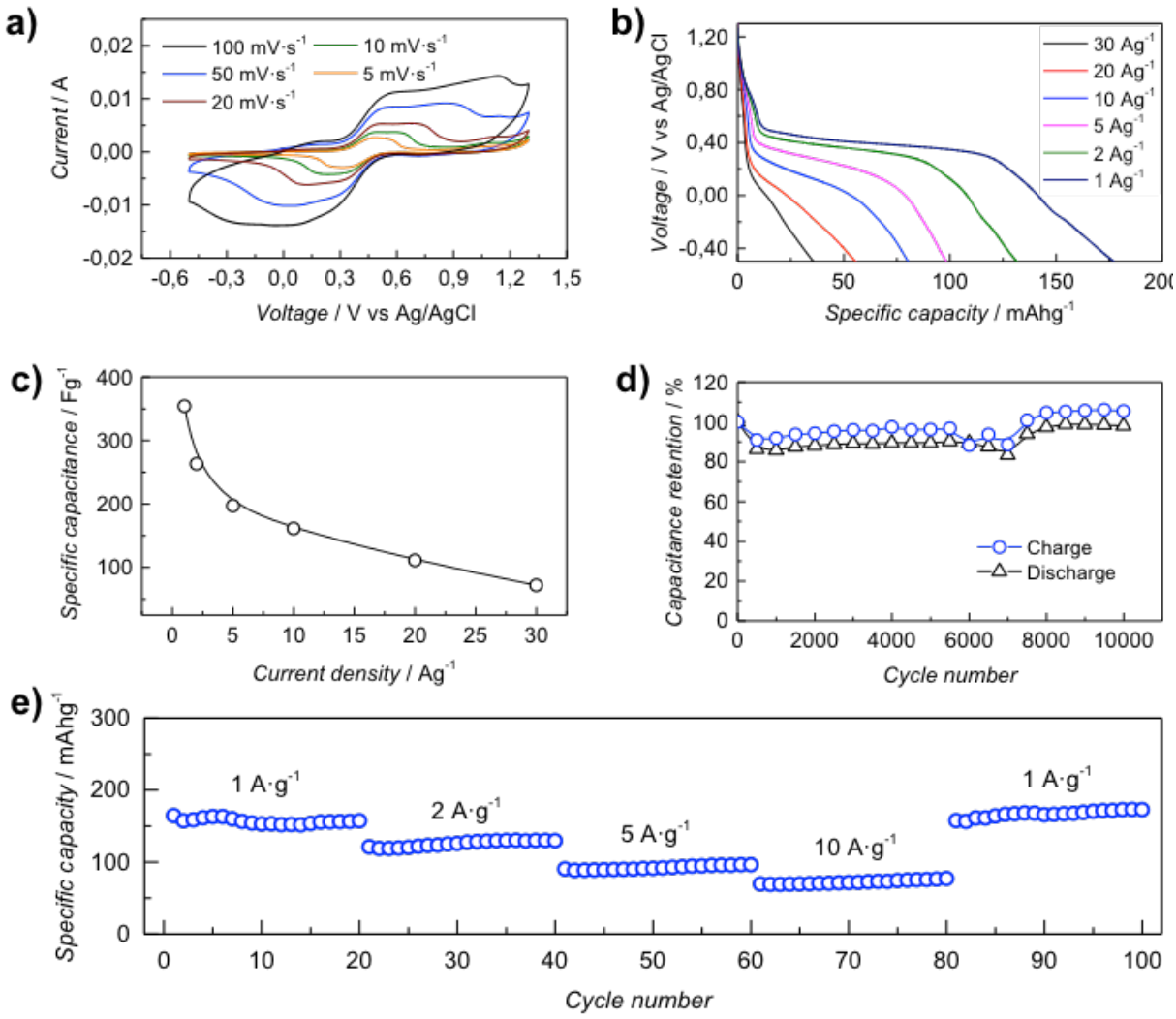

Figure 4. Electrochemical measurements of **1** in a typical three electrode cell using 1 M Na_2SO_4 aqueous solution. (a) CV at different scan rates. (b) Galvanostatic discharge curves at different current densities. (c) Specific capacitance at different discharge current densities. (d) Capacity retention in 10 000 charge–discharge cycles. (e) Rate capability at current rates ranging from 1 $A{\cdot}g^{-1}$ to 10 $A{\cdot}g^{-1}$.

Figure 4a shows the CVs of **1** in 1 M Na_2SO_4 aqueous electrolyte solution. CVs show two pairs of redox processes located between 0.2 V and 0.5 V that, according to the literature, [12,55,56] are assigned to the oxidation and reduction of the Fe atoms coordinated by the C atom in the cyanide ligand (Fe^{II}–CN) and the Fe atoms coordinated by the N atom (Fe^{III}–NC), respectively. The presence of the second peak, although not clearly resolved probably due to a partial pseudocapacitive behavior of the 2D composite shows that contrary to what commonly observed, Fe^{III} electrochemical activity is not blocked due to the presence of neighboring

vacancies and contributes to total specific capacity.[14] Most importantly, these peaks match well with the main potential plateau at the discharge curves (**Figure 4b**). Additionally, a plot of log (I) vs log (V) (**Figure S27**) provides an almost perfect linear dependence. A *b* value close to 0.5 for Na^+ insertion strongly suggests that electroactive material reactions are mainly controlled by Na^+ ion diffusion steps associated with the Na^+ ion concentration in the lattice, as has been reported previously.[57] After pre-activation, discharge capacity values up to 177 $mA{\cdot}h{\cdot}g^{-1}$ were obtained at current density of 1 $A{\cdot}g^{-1}$, reaching a specific capacitance of 354 $F{\cdot}g^{-1}$ (**Figure 4c**), which evidences an excellent material performance (**Table S5** and references therein).[13,14] As expected, under high current densities the specific capacities of the composite decrease rapidly.

It is worth noting that the charge and discharge capacity follow similar trends during the whole cycling experiment and that capacity remains steady with an outstanding capacity retention of ~98% after 10 000 charge-discharge cycles at a current density of 10 $A{\cdot}g^{-1}$ (as shown in **Figure 4d**). Thus the calculated round-trip efficiency is 98.3% at the first cycle and 91.3% at cycle 10 000. Moreover, rate capability was measured from 1 $A{\cdot}g^{-1}$ to 10 $A{\cdot}g^{-1}$ (**Figure 4e**). The electrode shows an excellent capacity retention even if the current density increased. Furthermore, the capacity recovered when the current density was lowered again to 1 $A{\cdot}g^{-1}$, suggesting the presence of reversible reactions. The long-life cycling performance and excellent rate capability of **1** suggest a high structural and electrochemical stability for Na-storage reactions.

Experiments performed when decreasing the Na^+ concentration in the aqueous electrolyte solution (0.5 M Na_2SO_4) present lower current values and differences in the width of the peaks, as previously described for thin films of PB analogues (**Figure S24**). [58] In fact, discharge capacity (**Figure S25**) and specific capacitance values (**Figure S26**) are much lower than those obtained in 1 M Na_2SO_4 solution (discharge capacity value at 1 $A{\cdot}g^{-1}$ of 105

mA·h·g^{-1} and specific capacitance of 210 F·g^{-1}). A mix of redox and intercalation pseudocapacitance render this material a highly promising cathode material for SIBs. [59]

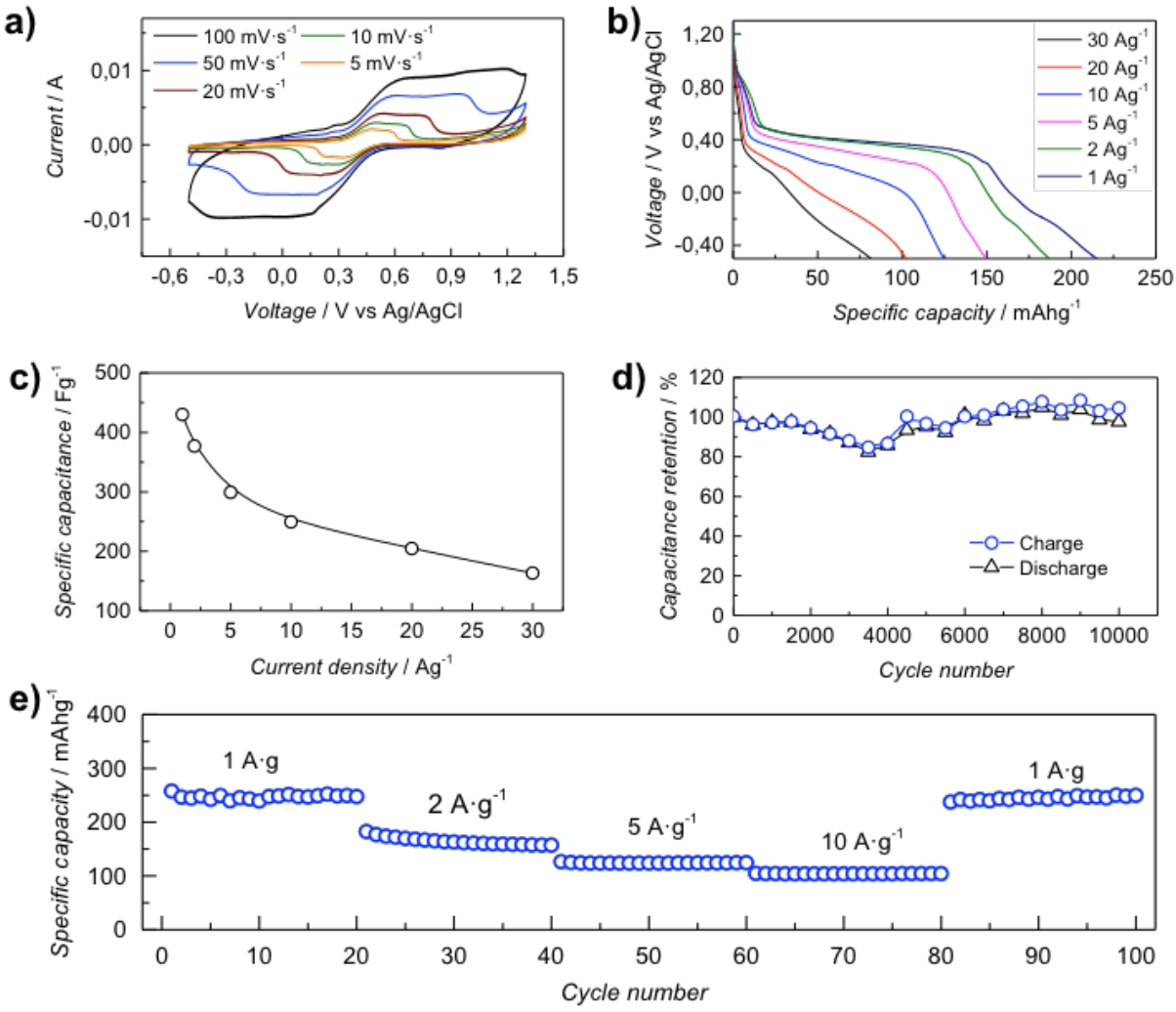

Figure 5. Electrochemical measurements of **1** in a typical three electrode cell using 0.5 M K_2SO_4 aqueous solution. (a) CV at different scan rates. (b) Galvanostatic discharge curves at different current densities. (c) Specific capacitance at different discharge current densities. (d) Capacity retention in 10 000 charge–discharge cycles. (e) Rate capability at current rates ranging from 1 A·g^{-1} to 10 A·g^{-1}.

Remarkably, when replacing Na^+ by K^+ (0.5 M K_2SO_4 electrolyte solution), although the CV curves look very similar to that obtained in 1 M Na_2SO_4 solution (**Figure 5a**), the values achieved by the discharge curves are considerably higher than those using Na^+ (**Figure 5b**): 215 mA·h·g^{-1} at 1 A·g^{-1} with specific capacitance up to 489 F·g^{-1} (**Figure 5c**), even larger than those achieved with a 1 M Na^+ electrolyte (177 mA·h·g^{-1} and 354 F·g^{-1}). In this case,

capacity also remains stable, with a capacity retention of ~97% after 10 000 charge-discharge cycles at a current density of 10 $A \cdot g^{-1}$, a value very close to the one obtained with sodium, as can be seen in **Figure 5d**. Thus the calculated round-trip efficiency is 95.9 % at the first cycle and 90.0 % at cycle 10 000. As well as in the sodium behavior, a similar rate capability is obtained, with higher values of the specific capacitance (**Figure 5e**). Here again, the electrode current changes with scan rate following an exponential order expected for a diffusion-controlled process (**Figure S28**). This indicates that electroactive material reactions are mainly controlled by K^+ diffusion.

The stability of **1** upon alkaline ions intercalation/de-intercalation was evaluated by the chemical characterization of the working electrode material after 200 charge/discharge cycles in 0.5 M K_2SO_4 aqueous solution. PXRD and XPS data are comparable to those obtained before the activation and clearly confirm the stability of the PB component and the underlying 2D material (Figure **S31**).

Next, the electrochemical properties of the KIB electrode were tested using electrochemical impedance spectroscopy (EIS) experiments before and after the charge/discharge cycling electrochemical treatment. The Nyquist diagram of the untreated electrode shows a classical behavior exhibiting a semicircle at high frequencies and a diffusional region at medium and low frequencies (see figure **S29** in the supporting information). The lower frequencies within the diffusion region show a slope of 50 degree near the theoretical value of 45 degree for a purely semi-infinite diffusion. An equivalent circuit depicted in figure S29D fits well with the experimental values in order to address the internal resistance regarding the migration of ions through the three-dimensional carbon felt electrode (see fitting in figure S29C using the equivalent circuit shown in figure S29D). Moreover, a transition from semi-infinite to finite diffusion is observed at low frequencies which are typical for porous electrodes. Owing to the intrinsic macroporosity and heterogeneity of the carbon felt electrode that adds a remarkable difficulty in the interpretation of the impedance results, EIS experiment of the pristine carbon

felt in the absence of the composite was also performed under the same EIS experimental conditions (see Figure **S30** in the supporting information). It is worth noticing that the onset of the diffusion region for the pristine carbon felt does not respond to a purely diffusion process, showing a slope superior to 60 degrees, when compared with the EIS behavior of the untreated electrode.

After the activation of the electrode by subjecting it to 50 charges/discharges cycles, a different EIS behavior is observed for the Nyquist diagram at high and moderate frequencies, as depicted in **Figure 6**, clearly showing a Nyquist diagram very representative for Na-ion kinetics in graphitized carbon electrodes.[60] We also used the representative equivalent circuit depicted in Figure 6d, which involves the appearance of two well defined semicircles at high and moderate frequencies, respectively, in contrast to the EIS behavior of the non-activated electrode. Accordingly, Q2 and R2 elements stand for the capacitance and resistance of the surface layer or passivating film (first semicircle), whereas the second semicircle is assumed to be related to charge transfer, though adsorption processes might also be taken into consideration.[61] Moreover, the onset of the diffusion region exhibits a slope 50 degrees again near a purely semi-infinite process. Hence, charges/discharges cycling of the electrode resulted to the appearance of two well defined physical phenome in the region of high and moderate frequencies similar to those presented in ion insertion into carbonaceous electrodes during battery charging.

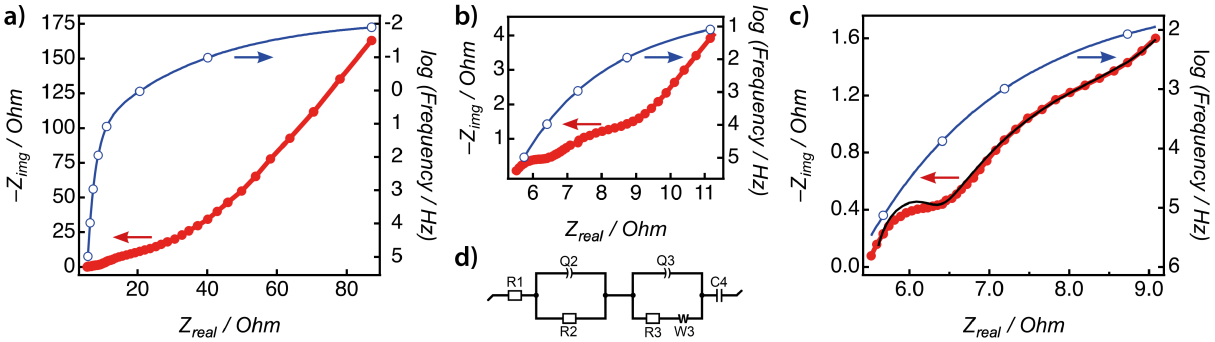

Figure 6. AC impedance diagram of the NIB cathode after 50 charge/discharge cycles in o.5 M K_2SO_4 aqueous solution. The frequency id given in a logarithmic scale in the graph and a line is drawn as gide for the eye. (b) Zoom of the high frequencies in (a). (c) Fit for the equivalen circuit described in the scheme (d). Frequency range for the experiment: 0.2 MHz – 10 mHz and for the fit: 0.2 MHz – 100 Hz. X^2 is least for the model (0.1225).

3. Discussion

We attribute the outstanding performance of **1** as cathode material for SIBs or KIBs to its atypical morphology, where the original 2D layer is fully covered by a continuous shell of nanometric-size PB crystals, as a result of the rapid nucleation and growth of the PB on the surface of the previously reduced MoS_2. This yields a crystalline material with optimum grain size[30] and increased surface area according to PXRD and gas sorption measurements respectively. This particular morphology improves accessibility to the voids and Na^+/K^+ diffusion during the charge/discharge processes, thus reducing maximum diffusion length, facilitating Fe^{III} and double-layer contributions to the overall capacitance and promoting a closer contact between the carbon matrix and the PB crystals. It is worthwhile noting that we cannot discard a potential contribution of the underlying 2D material to the cathode performance, as the activity of MoS_2 and MoO_x bulk and exfoliated materials for different energy storage processes has been largely demonstrated.[22,62] In operando studies will be performed in the near future in order to ascertain the contribution to the alkaline ion storage mechanism by each of the individual components in the composite. We attribute the good cyclability to the combination of the increased long-term resilience brought by the 2D matrix with the alleviated strain induced by volume changes during metalation/demetalation in our smaller crystals. Finally, the improvement observed when a K^+ electrolyte solution is used,

can be justified by the fact that the PB is synthetized from $K_3Fe(CN)_6$. This probably determines more optimum conditions for the diffusion and accommodation of K^+ ions *vs* Na^+ ions within the voids. Thus, the preparation of the composite using sodium hexacyanoferrate as precursor could be a key strategy to upgrade the performance of the material in Na^+ electrolyte solution for its future application in SIBs.

4. Conclusions

In summary, in this paper we have reported a straightforward approach for the preparation of PB/MoS_2 based composites with great potential for more efficient green energy batteries, both as powder samples and directly on surfaces. Chemically exfoliated MoS_2 provided a conductive matrix for the formation of the composite and its negative surface charge played a key role in the homogeneous growth of a high surface area PB particles that combines highly porosity and small crystal size. According to our electrochemical studies, more favorable diffusion of alkali cations along with the effective pseudocapacitive contribution from the 2D material results in a PB/2D composite with the highest value of specific capacitance reported up to date. These results highlight the synergistic behavior of these two electroactive components in the composite, prove the great potential of **1** as cathode material for SIBs and KIBs, and open the door to the combination of other TMDCs and PBAs for energy storage composites. The fact that PB could be nucleated on rMoS_2 networks directly over large areas, gives access to the integration of **1**, in 3D electrodes structured by physical techniques like Reactive Ion Etching (RIE) or Inductively Coupled Plasma (ICP). This will allow to produce electrodes with complex 3D patterns, in a low temperature CMOS compatible process, as well as achieving an increase of the stored charge without increasing the required volume, which is highly desirable in the search for systems that combine a reduced size and a high capacity.

5. Experimental Section ((delete section if not applicable))

Materials: Molybdenum(IV) sulfide was adquired from Alfa Aesar. *n*-butyllithium solution 1.6 M in hexane, iron(III) chloride, and potassium hexacyanoferrate(III) were purchased from Sigma-Aldrich. Solvents were used without further purification. Hydrochloric acid (37%) was purchased from Scharlau. Milli-Q water was used in all the experiments. SiO_2 (285 nm)/Si substrates were bought from NOVA Electronic Materials LLC, Flower Mound, TX, USA.

Intercalation/Chemical exfoliation of MoS_2: A lithium solvothermal intercalation method based on that reported by Zhou et al. [63] was used (see supporting information).

*Synthesis of the composite **1***: Potassium hexacyanoferrate(III) (164.6 mg, 0.5 mol) in 10 mL of water was slowly added to 10 mL of iron(III) chloride (81.1 mg, 0.5 mol,) in HCl 0.01 M. Afterwards, 6 mg of freshly dispersed chemically exfoliated MoS_2 flakes in water were dropped into the previous solution and stirred for 15 min. Next, the final mixture was filtered and washed with abundant water to remove the unreacted PB precursors. The obtained solid was dried under vacuum at room temperature for 1 h and stored in the dark before further characterizations.

*Non-covalent functionalization of micromechanically exfoliated MoS_2 flakes on surface (samples **2** and **3**):* Commercial MoS_2 flakes were micromechanically deposited onto a clean SiO_2 (285)/Si substrate using physical methods.[64] Next, samples were introduced in a glove box. Sample 2 was immersed in *n*-BuLi (1.6 M in hexane). After 24 h, it was immersed in hexane, ethanol, and isopropanol and dried with a N_2 stream. Afterwards, in ambient conditions, 2 mL of the above $K_3Fe(CN)_6$: $FeCl_3$ solution was drop casted onto the modified substrate for 15 s and then spin-coated at 3000 rpm for 1 min. For sample **3**, the same procedure was followed except for the *n*-BuLi treatment.

Non-covalent functionalization of chemically exfoliated MoS_2 flakes on surface (samples 4 and 5): A fresh suspension of MoS_2 flakes was spin-coated onto a clean SiO_2/Si substrate at 3000 rpm for 1 min. The resulting rMoS_2 network was functionalized with PB following the

same procedure described above for sample **3**. For sample **5**, 2.5 times more diluted $K_3Fe(CN)_6$: $FeCl_3$ solution was drop casted onto the modified substrate for 5 s and then spin-coated at 3000 rpm for 0.5 min.

Electrochemical measurements: For the electrochemical measurements, a mixture of **1**, acetylene black and PVDF in ethanol in a mass ratio of 80:10:10 was prepared and deposited on a carbon felt electrode previously calcinated at 1000 ºC. The as-prepared carbon felt was dried for two hours at 80 °C. The stability of the PB after the electrode preparation process was confirmed by PXRD. Each working electrode contained about 1 mg of electroactive material and had a geometric surface area of about 1 cm^2. A typical three-electrode cell equipped with a steel sheet as the counter electrode and a Metrohm Ag/AgCl (3 M KCl) as the reference electrode was used for the electrochemical characterization of the nanocomposite material trapped by the working electrodes. The electrochemical measurements were carried out in three different aqueous solutions (1 M and 0.5 M Na_2SO_4 and 0.5 M K_2SO_4) as the electrolytes. All the electrochemical experiments were performed at room temperature using a Gamry 1000E potentiostat–galvanostat controlled by Gamry software. The specific capacitance (C) was calculated from the cyclic chronopotentiometric curves according to $C = I\Delta t/m\Delta V$ where I is the charge/discharge current, Δt is the time for a full charge or discharge, m *is* the weight in grams of the active material in the electrode layer, and Δ is the voltage change after a full charge or discharge.

Electrode characterization was also performed by EIS. The measurements were performed using a VMP3 multichannel potentiostat-galvanostat BioLogic Science Instruments with a three-electrode electrochemical cell as described above. The impedance spectra were measured at a formal potential of 0.25 V *vs* AgCl/Ag (3.5 M KCl) over a frequency range between 10 mHz and 0.2 MHz with an amplitude potential of 0.010 V. A solution of 0.5 M K_2SO_4 was used as electrolyte and all impedance spectra was monitored at room temperature. Before the impedance measurements an equilibration time was required to reach an open

circuit potential until a constant value of 0.25 V which is almost in agreement with the formal potential of the first redox couple shown by cyclic voltammetry in Figure 5a. The impedance data was fitted by using the BioLogic software.

Powder X-ray Diffraction (XRD): Samples were filled into 1-mm-diameter borosilicate glass capillaries prior to being mounted and aligned on an Empyrean PANalytical powder diffractometer, using Cu Kα radiation (λ = 1.54056 Å) with an PIXcel detector, operating at 40 mA and 45 kV. At least three repeated measurements were collected at room temperature (2θ = 2–80°) range with a step size of 0.017° at room temperature and merged in a single diffractogram. Li_xMoS_2 capillaries were sealed in an inert atmosphere prior to analysis. Unit cell parameters values were calculated by Pawley refinement of experimental PXRD data as implemented in HighScore Plus©.

UV/Vis Spectroscopy: UV-vis absorption spectra were recorded on a Jasco V-670 spectrophotometer in baseline mode from 190 to 1200 nm range, using 1.000-cm-optical-path quartz cuvettes.

Raman Spectroscopy: Raman spectra of all the samples were acquired with a Raman Emission Horiba-MTB Xplora Spectrometer in ambient conditions. **1** was measured as a pellet (compressed powder) with a laser wavelength of 638 nm in order to preserve the stability of the sample during the measurement. The rest of samples were recorded with a laser wavelength of 532 nm.

High resolution transmission electron microscopy (HRTEM): HRTEM studies were carried out on a Technai G2 F20 microscope operating at 200 kV. Samples were prepared by dropping suspensions on lacey formvar/carbon copper grids (300 mesh). The employed suspensions were prepared by two different methods: by diluting an aliquot of the mother MoS_2 suspension in water and dispersing a little amount of the composite 1 in Milli-Q water.

Field Emission Scanning Electron Microscopy (FESEM): FESEM studies were performed on a Hitachi S-4800 microscope operating at an accelerating voltage of 20 kV and without metallization of the samples.

Atomic Force Microscopy (AFM): The substrates were imaged with a Digital Instruments Veeco Nanoscope IVa AFM microscope in tapping mode, using silicon tips with resonance frequency of 300 kHz and with an equivalent constant force of 40 N/m. AFM images were treated with Gwyddion [65] and WSxM softwares. [66]

Fourier Transform Infrared Spectroscopy (FT-IR): FT-IR spectra were recorded by a FT-IR Nicolet 5700 spectrometer (Thermo Scientific, Waltham, MA, USA, EEUU) in the 4000–400 cm^{-1} range using KBr pellets.

Inductively Coupled-Plasma Optical Emission Spectrometry (ICP-OES): The ICP-OES analysis of composite **1** was conducted at the Universidad Complutense de Madrid (CAI de Técnicas Geológicas). Samples were digested in a mixture of hydrocloridric and nitric acids using a high-pressure microwave oven.

Zeta Potential (ZP) measurements: Zeta potential measurements were performed at room temperature with a Zetasizer Nano ZS instrument (Malvern Instruments Ltd.).

Analysis of N_2 adsorption/desorption isotherms at 77 K: Gas adsorption measurements were carried out with Micromeritics 3Flex after activation of the solids at 425 K and 10^{-6} mbar for 16 h by using a Smart VacPrep unit. Surface area, pore size and volume values were calculated from nitrogen adsorption-desorption isotherms (77 K). Specific surface area (SA) was calculated by multi-point Brunauer-Emmett-Teller (BET) method. Total pore volume was calculated at $P/P_0 = 0.96$. Pore size distribution was analysed by using the solid density functional theory (NLDFT) for the adsorption branch assuming a cylindrical pore model with SAIEUS.

Mössbauer spectroscopy: Mössbauer spectra were collected at room temperature in transmission mode using a conventional constant-acceleration spectrometer and a 25 mCi

^{57}Co source in a Rh matrix in three different samples. The velocity scale was calibrated using α-Fe foil. Isomer shifts, *IS*, are given relative to this standard at room temperature. The absorber was obtained by packing the powdered samples into a perspex holder. The spectra were fitted to Lorentzian lines using a non-linear least-squares method. [67] The areas and widths of both peaks in a quadrupole doublet were constrained to remain equal during the refinement procedure.

Thermogravimetric analysis (TGA): Thermogravimetric analysis was conducted at the Universidad de Alicante (Unidad de Análisis Térmico y Sólidos Porosos) and was carried out with a Mettler Toledo TGA/SDTA851/1100/SF apparatus in the 25–600 °C temperature range under a 5 °C min^{-1} scan rate and N_2 flow of 100 mL min^{-1}.

Elemental CNS analysis: CNS analysis was performed by elementary analyser AE CHNS1110 CEInstruments, using a thermal conductivity detector. Helium and oxygen (both purity 99.995%) were used as the carrier and combusting gases, respectively. Combustion tube was set up at 1027 °C and reduction tube at 600 °C. Sulfanilamide was used as CHNS standard.

X-ray Photoelectron Spectroscopy (XPS): Samples were analysed ex situ at the X-ray Spectroscopy Service at the Universidad de Alicante using a K-ALPHA Thermo Scientific spectrometer. All spectra were collected using Al Kα radiation (1486.6 eV), monochromatized by a twin crystal monochromator, yielding a focused X-ray spot (elliptical in shape with a major axis length of 400 μm) at 30 mA and 2 kV. The alpha hemispherical analyzer was operated in the constant energy mode with survey scan pass energies of 200 eV to measure the whole energy band and 50 eV in a narrow scan to selectively measure the particular elements. XPS data were analyzed with Avantage software. A smart background function was used to approximate the experimental backgrounds. Charge compensation was achieved with the system flood gun that provides low energy electrons and low energy argon

ions from a single source. Commercial MoS_2 sample was used as reference (Mo $3d_{5/2}$ = 229.1 eV).

Magnetic measurements: Magnetic data was collected with a Quantum Design MPMS XL-5 susceptometer equipped with a SQUID sensor. *Dc* FC and ZFC magnetization measurements were performed under 100 Oe applied magnetic field. *Ac* magnetic susceptibility measurements were collected in the 2-8 K range at zero *dc* field and an applied oscillating field of 5 Oe at different frequencies.

Transport measurements: IV curves were measured using interdigitated pre-patterned Au electrodes (Fraunhofer IPMS) with a channel length of 10 μm and measured in a probe station using a Yokogawa GS200 voltage source and a Keithley 6517B electrometer. When necessary, system was dynamically pumped down to 10^{-6} mbar.

Supporting Information ((delete if not applicable))
Supporting Information is available from the Wiley Online Library or from the author.

Acknowledgements

R. Sanchis-Gual and J. Romero contributed equally to this work. We are very grateful to Prof. Jesus Iniesta and Prof. Vicente Montiel from the Institute of Electrochemistry, (Universidad de Alicante) for their helpful discussion about electrochemical characterization of the material. We acknowledge the financial support from the Spanish MINECO (MAT2014-56143-R co-financed by FEDER and Excellence Unit "María de Maeztu" MDM-2015-0538), the EU (ERC Proof of Concept Hy-MAC (713704), 2D-INK- (664878) and ERC Stg Chem-fs-MOF (714122)) and the Generalidad Valenciana (Prometeo Program). M. M.-G. and J. R. thanks the Spanish MINECO for the F.P.U. and F.P.I fellowships respectively, M. G. acknowledges the European Union Horizon 2020 Marie Curie Actions under the project SPIN2D (H2020/2014-659378) and A.F.-A. thanks the Universitat de València for a Research grant.

Received: ((will be filled in by the editorial staff))
Revised: ((will be filled in by the editorial staff))
Published online: ((will be filled in by the editorial staff))

References

[1] Y. Nishi, *J. Power Sources* **2001**, *100*, 101.
[2] L. Wu, W. H. Lee, J. Zhang, *Mater. Today* **2014**, *1*, 82.
[3] N. Yabuuchi, K. Kubota, M. Dahbi, S. Komaba, *Chem. Rev.* **2014**, *114*, 11636.
[4] Y. Liu, D. He, R. Han, G. Wei, Y. Qiao, *Chem. Commun. VL - IS* - **2017**, *53*, 1.
[5] J.-Y. Hwang, S.-T. Myung, Y.-K. Sun, *Chem. Soc. Rev.* **2017**, *46*, 3529.
[6] H. Buser, D. Schwarzenbach, W. Petter, A. Ludi, *Inorg. Chem.* **1977**, *16*, 2704.
[7] K. R. Dunbar, R. A. Heintz, In *Progress in Inorganic Chemistry*; Progress in Inorganic Chemistry; John Wiley & Sons, Inc.: Hoboken, NJ, USA, 1996; Vol. 45, pp. 283–391.
[8] H.-W. Lee, R. Y. Wang, M. Pasta, S. W. Lee, N. Liu, Y. Cui, *Nat. Commun.* **2014**, *5*, 5280.
[9] Y. You, X.-L. Wu, Y.-X. Yin, Y.-G. Guo, *Energy Environ. Sci.* **2014**, *7*, 1643.
[10] X. Wu, Z. Jian, Z. Li, X. Ji, *Electrochemistry Communications* **2017**, *77*, 54.
[11] Y. Yue, A. J. Binder, B. Guo, Z. Zhang, Z.-A. Qiao, C. Tian, S. Dai, *Angew. Chem. Int. Ed.* **2014**, *53*, 3134.
[12] Y. Lu, L. Wang, J. Cheng, J. B. Goodenough, *Chem. Commun. VL - IS* - **2012**, *48*, 6544.
[13] S. J. R. Prabakar, J. Jeong, M. Pyo, *RSC Adv.* **2015**, *5*, 37545.
[14] Y. Jiang, S. Yu, B. Wang, Y. Li, W. Sun, Y. Lu, M. Yan, B. Song, S. Dou, *Adv. Funct. Mater.* **2016**, *26*, 5315.
[15] L. Cao, Y. Liu, B. Zhang, L. Lu, *ACS Appl. Mater. Interfaces* **2010**, *2*, 2339.
[16] L. Zhang, A. Zhang, D. Du, Y. Lin, *Nanoscale* **2012**, *4*, 4674.
[17] J.-G. Wang, Z. Zhang, X. Liu, B. Wei, *Electrochim. Acta* **2017**, *235*, 114.
[18] M. Zhang, C. Hou, A. Halder, J. Ulstrup, Q. Chi, *Biosens. Bioelectron.* **2017**, *89*, 570.
[19] H. Wang, L. Wang, S. Chen, G. Li, J. Quan, E. Xu, L. Song, Y. Jiang, *J. Mater. Chem. A* **2017**, *5*, 3569.
[20] C. Tan, X. Cao, X.-J. Wu, Q. He, J. Yang, X. Zhang, J. Chen, W. Zhao, S. Han, G.-H. Nam, M. Sindoro, H. Zhang, *Chem. Rev.* **2017**, *117*, 6225.
[21] Q. H. Wang, K. Kalantar-Zadeh, A. Kis, J. N. Coleman, M. S. Strano, *Nat Nano* **2012**, *7*, 699.
[22] T. Wang, S. Chen, H. Pang, H. Xue, Y. Yu, *Adv. Sci.* **2016**, *4*, 1600289.
[23] P. Joensen, R. F. Frindt, S. R. Morrison, *Mat. Res. Bull.* **1986**, *21*, 457.
[24] D. Voiry, A. Goswami, R. Kappera, C. de Carvalho Castro e Silva, D. Kaplan, T. Fujita, M. Chen, T. Asefa, M. Chhowalla, *Nat. Chem.* **2014**, *7*, 45.
[25] K. C. Knirsch, N. C. Berner, H. C. Nerl, C. S. Cucinotta, Z. Gholamvand, N. McEvoy, Z. Wang, I. Abramovic, P. Vecera, M. Halik, S. Sanvito, G. S. Duesberg, V. Nicolosi, F. Hauke, A. Hirsch, J. N. Coleman, C. Backes, *ACS Nano* **2015**, *9*, 6018.
[26] J. Kim, S. Byun, A. J. Smith, J. Yu, J. Huang, *J. Phys. Chem. Lett.* **2013**, *4*, 1227.
[27] S. Su, X. Han, Z. Lu, W. Liu, D. Zhu, J. Chao, C. Fan, L. Wang, S. Song, L. Weng, L. Wang, *ACS Appl. Mater. Interfaces* **2017**, *9*, 12773.
[28] Y. V. Lim, Y. Wang, L. Guo, D. Kong, R. Ang, J. I. wong, H. Y. Yang, *J. Mater.*

Chem. A **2017**, 1.
[29] A. Gupta, V. Arunachalam, S. Vasudevan, *J. Phys. Chem. Lett.* **2015**, *6*, 739.
[30] H. Ming, N. L. K. Torad, Y.-D. Chiang, K. C. W. Wu, Y. Yamauchi, *CrystEngComm* **2012**, *14*, 3387.
[31] L. Samain, F. Grandjean, G. J. Long, P. Martinetto, P. Bordet, D. Strivay, *J. Phys. Chem. C* **2013**, *117*, 9693.
[32] M. M. Barsan, I. S. Butler, J. Fitzpatrick, D. F. R. Gilson, *J. Raman Spectrosc.* **2011**, *42*, 1820.
[33] E. Nossol, V. H. R. Souza, A. J. G. Zarbin, *Journal of Colloid and Interface Science* **2016**, *478*, 107.
[34] F. Grandjean, L. Samain, G. J. Long, *Dalton Trans.* **2016**, *45*, 18018.
[35] S. N. Ghosh, *J. Inorg. Nucl. Chem.* **1974**, *36*, 2465.
[36] G. Wang, G. Zhang, H. Huang, L. Wang, *Anal. Methods* **2011**, *3*, 2082.
[37] N. N. Greenwood, T.C. Gibb, *Mössbauer Spectroscopy*, Chapman and Hall, Ltd. Publishers, London, UK **1971**
[38] D. W. Kim, J. M. Ok, W.-B. Jung, J.-S. Kim, S. J. Kim, H. O. Choi, Y. H. Kim, H.-T. Jung, *Nano Lett.* **2015**, *15*, 229.
[39] G. L. Frey, K. J. Reynolds, R. H. Friend, H. Cohen, Y. Feldman, *J. Am. Chem. Soc.* **2003**, *125*, 5998.
[40] S. S. Chou, Y.-K. Huang, J. Kim, B. Kaehr, B. M. Foley, P. Lu, C. Dykstra, P. E. Hopkins, C. J. Brinker, J. Huang, V. P. Dravid, *J. Am. Chem. Soc.* **2015**, *137*, 1742.
[41] C. X. Zhou, Y. X. Wang, L. Q. Yang, J. H. Lin, *Inorg. Chem.* **2001**, *40*, 1521.
[42] X. K. Hu, Y. T. Qian, Z. T. Song, J. R. Huang, R. Cao, J. Q. Xiao, *Chem. Mater.* **2008**, *20*, 1527.
[43] Y. Hu, D. H. C. Chua, *Sci. Rep.* **2016**, *6*, 28088.
[44] T. Uemura, S. Kitagawa, *J. Am. Chem. Soc.* **2003**, *125*, 7814.
[45] H. Li, J. Wu, Z. Yin, H. Zhang, *Acc. Chem. Res.* **2014**, *47*, 1067.
[46] H. Li, Q. Zhang, C. C. R. Yap, B. K. Tay, T. H. T. Edwin, A. Olivier, D. Baillargeat, *Adv. Funct. Mater.* **2012**, *22*, 1385.
[47] Y. You, X. Yu, Y. Yin, K.-W. Nam, Y.-G. Guo, *Nano Res.* **2014**, *8*, 117.
[48] J. Zhao, Y. Zhang, C. Shi, H. Chen, L. Tong, T. Zhu, Z. Liu, *Thin Solid Films* **2006**, *515*, 1847.
[49] G. Niaura, A. Malinauskas, R. Mazeikien, *J. Electroanal. Chem.* **2011**, *660*, 140.
[50] Y. Xi, M. I. Serna, L. Cheng, Y. Gao, M. Baniasadi, R. Rodriguez-Davila, J. Kim, M. A. Quevedo-Lopez, M. Minary-Jolandan, *J. Mater. Chem. C* **2015**, *3*, 3842.
[51] J. S. Kim, J. Kim, J. Zhao, S. Kim, J. H. Lee, Y. Jin, H. Choi, B. H. Moon, J. J. Bae, Y. H. Lee, S. C. Lim, *ACS Nano* **2016**, *10*, 7500.
[52] S. Ganguli, M. Bhattacharya, *J. Chem. Soc., Faraday Trans. 1* **1983**, *79*, 1513.
[53] K. Tennakone, W. Dharmaratne, *J. Phys. C: Solid State Phys.* **1983**, *16*, 5633.
[54] D. M. Pajerowski, T. Watanabe, T. Yamamoto, Y. Einaga, *Phys. Rev. B Condens. Matter Mater. Phys.* **2011**, *83*, 153202.
[55] A. Pajor-Swierzy, T. Kruk, P. Warszy ski, *Colloids and Interface Science Communications* **2014**, *1*, 6.
[56] R. Hazen, R. M. Spaulding, K. K. Kasem, *Am. J. Undergrad. Res.* **2003**, *2*, 27.
[57] W. Wu, S. Shabhag, J. Chang, A. Rutt, J. F. Whitacre, *J. Electrochem. Soc.* **2015**, *162*, A803.
[58] S. Zamponi, M. Berrettoni, P. J. Kulesza, K. Miecznikowski, M. A. Malik, O. Makowski, R. Marassi, *Electrochim. Acta* **2003**, *48*, 4261.
[59] J. Wang, S. Dong, B. Ding, Y. Wang, X. Hao, H. Dou, Y. Xia, X. Zhang,

National Science Review **2017**, *4*, 71.
[60] V. F. Lvovich, *Impedance Spectroscopy: Applications to Electrochemical and Dielectric Phenomena*, Wiley, Hoboken, NJ, USA **2012**.
[61] S. Franger, S. Bach, J. Farcy, J. P. Pereira-Ramos, N. Baffier, *Electrochim. Acta* **2003**, *48*, 891.
[62] X. Hu, W. Zhang, X. Liu, Y. Mei, Y. Huang, *Chem. Soc. Rev.* **2015**, *44*, 2376.
[63] L. Zhou, B. He, Y. Yang, Y. He, *RSC Adv.* **2014**, *4*, 32570.
[64] K. S. Novoselov, A. K. Geim, S. V. Morozov, D. Jiang, Y. Zhang, S. V. Dubonos, I. V. Grigorieva, A. A. Firsov, *Science* **2004**, *306*, 666.
[65] D. Nečas, P. Klapetek, *Open Physics* **2011**, *10*, 181.
[66] I. Horcas, R. Fernández, J. M. Gómez-Rodríguez, J. Colchero, J. Gómez-Herrero, A. M. Baro, *Rev. Sci. Instrum.* **2007**, *78*, 013705.
[67] J. C. Waerenborgh, P. Salamakha, O. Sologub, A. P. Gonçalves, C. Cardoso, S. Sério, M. Godinho, M. Almeida, *Chem. Mater.* **2000**, *12*, 1743.

Table of Content

Chemically exfoliated MoS_2 has been used as active sheets for the synthesis of a Prussian blue-2D based composite, which behaves as a highly efficient material in sodium and potassium ion batteries. The coordination network forms highly porous nanoparticles, homogeneously distributed all over the molybdenum layers. This morphology provides structural resilience, favors ion diffusion and permits the double-layer contributions to the overall capacitance.

Keyword

Composite Materials, electrodes, batteries, surface modification

M. Morant-Giner, R. Sanchis-Gual, J. Romero, A. Alberola, L. García-Cruz, S. Agouram, M. Galbiati, N. M. Padial, J. C. Waerenborgh, C. Martí-Gastaldo, S. Tatay, A. Forment-Aliaga* and E. Coronado*

Title ((no stars))

Prussian blue@MoS_2 layer composites as highly efficient cathodes for sodium- and potassium-ion batteries.